Mapping Wetland Plant Communities Using Unmanned Aerial Vehicle Hyperspectral Imagery by Comparing Object/Pixel-Based Classifications Combining Multiple Machine-Learning Algorithms

Baojia Du, Dehua Mao, Zongming Wang, Zhiqiang Qiu, Hengqi Yan, Kaidong Feng, and Zhongbin Zhang

***Abstract*—Understanding the spatial patterns of plant communities is important for sustainable wetland ecosystem management and biodiversity conservation. With the rapid development of unmanned aerial vehicle (UAV) technology, UAV-borne hyperspectral data with high spatial resolution have become ideal for accurate classification of wetland plant communities. In this article, four dominant plant communities (*Phragmites australis*, *Typha orientalis*, *Suaeda glauca*, and *Scirpus triqueter*) and two unvegetated cover types (water and bare land) in the Momoge Ramsar wetland site were classified. This was achieved using UAV hyperspectral images and three object- and pixel-based machine-learning classification algorithms [random forest (RF), convolutional neural network (CNN), and support vector machine (SVM)]. First, spectral derivative analysis, logarithmic analysis, and continuum removal analysis identified the wavelength at which the greatest difference in reflectance occurs. Second, dimensionality reduction of hyperspectral images was conducted using principal component analysis. Subsequently, an optimal feature combination for community mapping was formed based on data transformation (spectral features, vegetation indices, and principal components). Image objects were obtained by segmenting the optimum object feature subsets. Finally, distribution maps of communities were produced by using three machine-learning classification algorithms. Our results reveal that object-based image analysis outperforms pixel-based methods, with overall accuracies (OAs) of 80.29–87.75%; RF has the highest OA of 87.75% (Kappa = 0.864), followed consecutively by CNN (OA = 83.31%, Kappa = 0.829) and SVM (OA = 80.29%, Kappa = 0.813). *Phragmites australis* dominates the plant community (55.9%) at the study area, followed by *Typha orientalis* (16.2%), *Suaeda glauca* (16.2%), and *Scirpus triqueter* (4.6%). The results highlight the importance of spectral transformation features in red-edge regions. The mapping results will help establish basic information for subsequent studies involving habitat suitability assessment at this study site.**

***Index Terms*—Community classification, hyperspectral remote sensing, machine learning, unmanned aerial vehicle (UAV), wetland.**

I. Introduction

WETLAND plants act as sentinels for ecological changes and provide early signs of physical or chemical degradation, such as reduction of wetland area and wetland plant diversity, decreased and damaged rare and endangered waterfowl habitats, water eutrophication, as well as decreased of organic matter accumulation and primary productivity [1], [2]. And once their health and functions are disturbed, the effects are detrimental on all life forms supported by wetlands [3]. Recognizing wetland plant communities and understanding their geospatial patterns are important for sustainable wetland ecosystem management and biodiversity conservation [4]. Traditional mapping of wetland plant communities requires intensive fieldwork that is labor-intensive, expensive, time-consuming, sometimes inapplicable because of limited accessibility, and so is only practical in relatively small areas. Instead, remote sensing provides a useful tool for identifying and mapping wetland plant communities over large spatial areas [5].

Since the late 1980s, the rapid development of satellite remote sensing technology has greatly enhanced our ability to delineate wetlands [6], [7]. However, because of their small number of spectral channels, traditional multispectral sensors have limited ability to identify wetland plant communities accurately [8], [9]. Although the spatial resolution of some satellite images has improved significantly (e.g., Quickbird and Worldview images), limitations in spectral resolution mean that the classification of wetland plant communities may be unsatisfactory

Manuscript received May 5, 2021; revised June 29, 2021 and July 13, 2021; accepted July 17, 2021. Date of publication July 30, 2021; date of current version September 1, 2021. This work was supported in part by the National Natural Science Foundation of China under Grant 41771383, in part by the Science and Technology Development Program of Jilin Province under Grant 20200301014RQ, and in part by the Scientific Research Instrument and Equipment Development Project of Chinese Academy of Sciences under Grant YJKYYQ2019004. *(Corresponding author: Dehua Mao.)*

Baojia Du, Zhiqiang Qiu, and Kaidong Feng are with the Key Laboratory of Wetland Ecology and Environment, Northeast Institute of Geography and Agroecology, Chinese Academy of Sciences, Changchun 130102, China, and also with the University of Chinese Academy of Sciences, Beijing 100049, China (e-mail: dubaojia@iga.ac.cn; qiuzhiqiang@iga.ac.cn; fengkaidong20@mails.ucas.ac.cn).

Dehua Mao is with the Key Laboratory of Wetland Ecology and Environment, Northeast Institute of Geography and Agroecology, Chinese Academy of Sciences, Changchun 130102, China, and also with the Changchun Jingyuetan Remote Sensing Observation Station, Chinese Academy of Sciences, Changchun 130102, China (e-mail: maodehua@iga.ac.cn).

Zongming Wang is with the Key Laboratory of Wetland Ecology and Environment, Northeast Institute of Geography and Agroecology, Chinese Academy of Sciences, Changchun 130102, China, and also with the National Earth System Science Data Center, Beijing 100101, China (e-mail: zongmingwang@iga.ac.cn).

Hengqi Yan is with the YanBian University, Yanji 133002, China (e-mail: yanhengqi1991@163.com).

Zhongbin Zhang is with the Jilin Geologic Surveying and Mapping Institute, Changchun 130062, China (e-mail: zzb0206@126.com).

Digital Object Identifier 10.1109/JSTARS.2021.3100923

[10], [11]. Hyperspectral images can capture the subtle spectral differences among ground objects because of the continuous spectral information, thereby allowing different wetland plant communities to be identified accurately [1], [12]. In recent years, hyperspectral data have been commonly used to map wetland plant communities by means of diverse algorithms [13], [14]. However, the application of hyperspectral imagery still has some limitations. First, there are relatively few hyperspectral data sources based on satellite platforms. Second, high-quality hyperspectral images are scarce because of weather conditions. Third, the effectiveness of space-borne hyperspectral imagery for mapping plant communities is limited by its coarse spatial resolution (i.e., 20–30 m or more) [15]. These problems make it difficult for wetland managers or researchers to use traditional hyperspectral remote sensing technology for real-time, flexible monitoring.

Compared with space platforms, unmanned aerial vehicles (UAVs) are cheaper and allow flight routes to be designed more flexibly [16]. As emerging low-altitude remote sensing platforms, UAV hyperspectral imaging systems have been used widely in various natural-resource management tasks, including classifying natural land cover [17], monitoring crop health [18], ecological research [19], and extracting the biophysical attributes of vegetation [20]. In recent years, UAV-hyperspectral sensing has recently gained traction in wetland plant communities monitoring studies. For instance, Cao *et al.* utilized spectral–textural features and vegetation indices (VIs) extracted from UAV hyperspectral images and support vector machine (SVM) to perform mangrove species identification in a coastal wetland environment [21]. Bikram *et al.* developed a preprocessing workflow for UAV-hyperspectral imaging of highly heterogeneous environments to address the specific issues of monitoring the heterogenous distribution of the swamp vegetation [22]. Compared with space-borne hyperspectral images, UAV hyperspectral imagery is an optimal remote sensing data source for mapping wetland communities, given that it combines high spatial–spectral resolution with acquisition timing. It can realize the rapid monitoring of natural vegetation under customized temporal and spatial scales. With reduced sensor costs and increased data storage capacity, hyperspectral sensors on UAVs will pave the way for more accurate monitoring of wetland plant communities.

Object-based classification methods have attracted increasing attention over recent years and have witnessed steady progress [17]. However, it is difficult to obtain higher classification accuracies when processing high-spatial-resolution hyperspectral images. First, the high dimensionality of spectral information produces the Hughes phenomenon [23], which can greatly reduce the classification accuracies. Second, the abundant information provided by high-resolution images may increase the intraclass differences and decrease the interclass differences in the spatial and spectral domains [24], resulting in lower interpretation accuracies. Third, because of the homogenization effect of water or dead-vegetation signals [25], the spectral similarity of different categories will reduce the classification accuracy and effectiveness. To extract effective information from hyperspectral imagery and improve classification efficiency, feature extraction and feature selection are usually used to reduce the data dimensions.

In terms of classification, machine-learning algorithms have demonstrated excellent performance for the analyses of many complex remote sensing datasets. Random forest (RF) is an ensemble learning technique, which is composed of multiple decision-making trees [26]. Moreover, RF is capable of measuring the importance of an individual input variable or a set of variables in the classification [27]. Convolutional neural network (CNN) is a deep-learning method that was designed especially for image classification and recognition based on multilayer neural networks [28]. The SVM algorithm finds the optimum minimization, i.e., the decision boundary of ambiguous classifier outputs in a problem space [29]. The basic idea of SVM algorithm is to convert the image into a high-dimensional space, perform linear fitting, and then determine the optimal linear classification surface [30]. In this article, the selected three machine-learning algorithms (RF, CNN, and SVM) have a rich and successful history in machine learning including applications in hyperspectral image classification. All algorithms used in this article are nonparametric methods, which do not require any prior assumptions about the statistical distribution of data, so they have an advantage over parametric algorithms [29], [31].

The Momoge National Nature Reserve (MNNR), a Ramsar wetland site in Northeast China, plays a key role in conserving wetland biodiversity and endangered waterbirds. The Momoge wetland harbors diverse wetland plant communities that provide a host of ecosystem services and benefits, but no specific mapping results for the wetland plant communities have been acquired to date, thereby limiting sustainable ecosystem management and biodiversity conservation. Aimed at meeting the demands of plant community monitoring over a core area of MNNR, this article uses UAV hyperspectral imagery with high spatial resolution to map wetland plant communities by comparing the accuracy of object-based and pixel-based approaches. The main objectives of this article are to 1) make full use of the high spatial characteristics and hyperspectrality of UAV hyperspectral images to realize the fine identification of different wetland plant community types and 2) examine the effectiveness of various machine-learning classification algorithms (RF, CNN, and SVM) for mapping wetland plant communities.

II. Materials and Methods

A. Study Area

The MNNR (45°42′25″–46°17′59″N, 123°27′09″–124°4′32″E) is located in the west of Jilin province in Northeast China, with an area of 14.4×10^4 hm^2 (Fig. 1). It was established in 1981 and listed in the National Nature Reserves of China in 1997 and the Ramsar site in 2013 [32]. There are 193 recorded bird species, and over 10 species of national class I protected birds in the MNNR. In addition, the 6 of 15 species of cranes in the world are found in the MNNR [33]. Many international organizations, such as the International Crane Foundation, the Global Environment Facility, and the World Wildlife Fund, particularly concerned about this area [34]. In

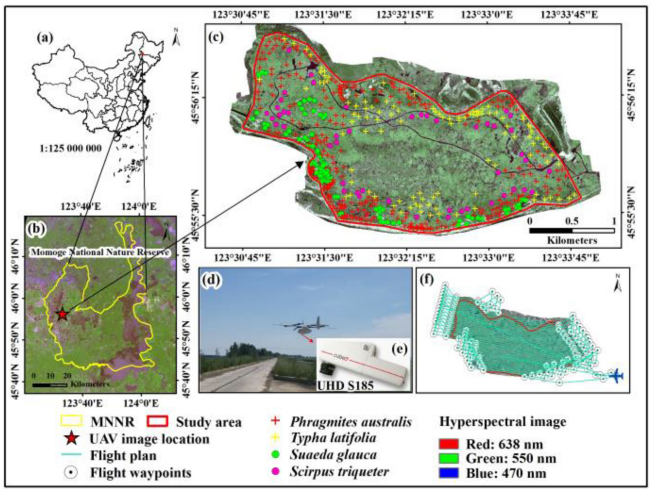

Fig. 1. Location of study site. (a) MNNR's position in China. (b) Sentinel-2 image of Momoge National Nature Reserve. (c) True-color RGB image of the UAV-borne hyperspectral data for the study area together with the location of sampling points. (d) Carrier platform fixed-wing unmanned aerial vehicle (CW-10 JOUAV) and image capture system with Cubert UHD S185 hyperspectral sensor. (e) UHD S185 hyperspectral sensor. (f) Flight plan and waypoints of fixed-wing aircraft.

TABLE I
MAIN PARAMETERS OF THE UHD 185 SNAPSHOT HYPERSPECTRAL SENSOR AND CW-10 UAV

UHD 185 hyperspectral camera		CW-10 JOUAV	
Wavelength range	450–950 nm	Wingspan	2.6 m
Total weight	470 g	Radio link	35 km
Field of view	19°	GPS	RTK/PPK
Image size	1000 × 1000	Payload	1-2 kg
Sampling interval	4 nm	Endurance	90 min
Spectral resolution	8 nm @ 532 nm	Cruise speed	72 km/h
Channels	125	Wind resistance	10-13 m/s
Spectral throught	2500 spectra/cube	Max takeoff altitude	3500 m
Detector	Si CCD	H positioning accuracy	1cm+1ppm
Digitization	12 bit	Ground control station	CW commander
Power	DC 12 V, 8 W		

the present study, a subset of the MNNR was chosen as the study area, as shown in Fig. 1.

B. UAV Hyperspectral Image Acquisition and Preprocessing

We used a CW-10 fixed-wing UAV (JOUAV, Sichuan, China) equipped with a UHD S185 hyperspectral sensor (Cubert GmbH, Ulm, Germany) to form the UAV hyperspectral imaging system. The parameters of the UHD S185 sensor and CW-10 UAV are presented in Table I. UHD S185 is a hyperspectral snapshot camera which provides 125 channels in a spectral range of 450 to 950 nm. For each band, a 50 by 50 pixel image with 12 bit (4096 DN) precision is created [36]. Additionally, a grayscale image with 1000 × 990 pixels is recorded simultaneously with the hyperspectral image using the same camera through the same lens [35]. Before data collection, a black-and-white board was used for radiation calibration of the UHD S185 hyperspectral sensor. It can obtain reflected radiation from the visible to near-infrared

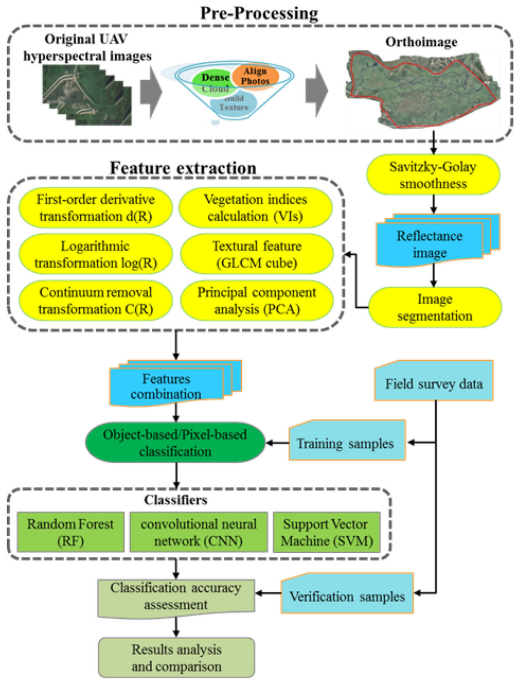

Fig. 2. Flowchart of wetland plant communities classification procedure.

spectra [37]. To obtain the reflectance values, the dark measurements were subtracted from the reference measurements and the actual measured values [21]. Hyperspectral imaging data were obtained under sunny and windless conditions on July 23, 2020. All the flights were executed between 10:00 and 14:00 local time. The image ground resolution was 15 cm. In Fig. 1, the range of the red border is the extent of the UAV hyperspectral data collection area, approximately 600 ha. The images were acquired at 70% transverse overlap and 80% forward overlap.

The preprocessing of the hyperspectral images involved mainly format conversion, photo alignment, and image fusion. The Cubert Cube-Pilot software version 1.4 (Cubert GmbH, Baden-Württemberg, Germany) was used to format conversion of the original data, and Agisoft PhotoScan software Version 1.2.5 (Agisoft, St. Petersburg, Russia) was used to photo alignment, image fusion, and generate a hyperspectral orthophoto map for the study area. The spatial resolution of the stitched hyperspectral images was about 15 cm. A detailed description of preprocessing methods of the hyperspectral images is provided by [38]. A flowchart is illustrated in Fig. 2.

C. Field Survey Dataset

We collected the field reference data of typical wetland plant communities in the study site during the flight mission. The coordinates of wetland plant community plots were recorded by a handheld differential global positioning system with submeter accuracy. According to these field investigations, *Phragmites australis*, *Typha orientalis*, *Suaeda glauca*, and *Scirpus triqueter* were the dominant wetland plant community types (Fig. 3). Based on the recorded field samples (each 1 m × 1 m), a total of 402 sample polygons (regions of interest) were outlined manually in the hyperspectral imagery. The numbers of training

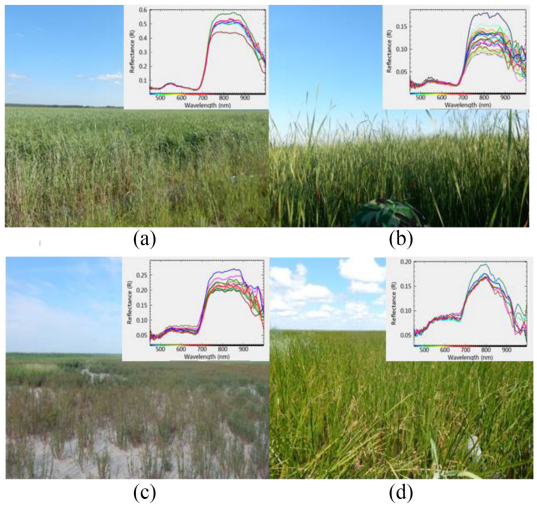

Fig. 3. Ground photos representing different wetland plant communities for the study site. The reflectance spectra of four wetland plant communities are taken from the UAV hyperspectral imagery located at each sampling plot.

TABLE II
NUMBER OF SAMPLES FOR TRAINING AND VALIDATION FOR EACH WETLAND PLANT COMMUNITIES

Wetland plant communities	Training Samples Polygons (number of pixels)	Validation Samples Polygons (number of pixels)
Phragmites australis	157(7693)	78(3822)
Typha latifolia	104(5096)	50(2450)
Suaeda glauca	93(4557)	46(2254)
Scirpus triqueter	88(4312)	40(1960)
Total	442(21658)	214(10486)

and verification sample polygons and the corresponding pixels of each wetland plant community are given in Table II.

D. Image Segmentation

Segmentation is the process used to divide the imagery into homogeneous image segments or objects [39]. The accuracy of image segmentation significantly affects the classification accuracy. Pretreated hyperspectral imagery in this article was segmented into object levels using the multiresolution segmentation method in eCognition Developer 9.3 (Trimble Germany Gmbh, Munich, Germany). The segmentation parameters tested in eCognition included scale, shape, and compactness [40]. A trial-and-error approach and visual inspection of the segmentation results was employed in order to determine which optimum segmentation parameters produced the most meaningful image objects, i.e., how well the image objects matched feature boundaries in the image [39]. When the segmentation scale was defined as 35 or 40, neighboring objects with similar features were generally mixed together. When the scale was set to 10 or 25, the segmentation results were too fragile, which would influence the efficiency of image processing. After a series of trial runs (e.g., scale: 5 to 50 with an increment of 5 each time; compactness: 0.1 to 1 with an increment of 0.05; shape: 0.1 to 1 with an increment of 0.05), the optimal segmentation scale, shape index, and compactness were set to 30, 0.4, and 0.5.

E. Feature Space Reduction

The high dimensionality of the hyperspectral data makes the classification problem more complex. High-dimensional data usually need feature selection before machine learning [41]. The feature selection was aimed at reducing processing times and developing ways to use less of the data but still be able to achieve satisfying results.

1) Data Transformation: Derivative transformation [d(R)] and logarithmic transformation [log(R)] are commonly utilized in hyperspectral analysis of plants, which can effectively reduce the influence of illumination variations, and eliminate the background signal and reveal the peak characteristics of the plant spectrum [48]. Furthermore, continuum-removal transformation [C(R)] can also enhance the spectral differences in the visible region. Therefore, four transformation of R [d(R), log(R), d[log(R)], and C(R)] were computed as

$$\mathrm{d}\left(\mathrm{R}\right) \approx \frac{\lambda\left(\lambda_i\right) - \cdots + \mathrm{R}\left(\lambda_{i+n}\right)}{\left(\Delta\lambda\right)^n} = \frac{\sum_i^{i+n} C_k \mathrm{R}\left(\lambda_k\right)}{\left(\Delta\lambda\right)^n} \quad (1)$$

$$\log\ \left(\mathrm{R}\right) = \left[\log\left(\lambda_1\right),\ \log\left(\lambda_2\right), \ldots, \log\left(\lambda_n\right)\right] \quad (2)$$

$$\mathrm{C\,R}_{j\in(\lambda_1,\lambda_2)} = \left|\left(\frac{\rho_j}{\rho_{ji}}\right) - 1\right| \quad (3)$$

where $j = (2i+n)\ /2$, if $(2i+n)$is even, or $j = (2i+n+1)\ /2$, if $(2i+n)$ is odd, and $\Delta\lambda$ denotes the double waveband intervals (nm); ρ_j is measured reflectance of a band j; ρ_{ji} is the reflectance of the same band linearly interpolated within the predefined wavelength interval of $(\lambda_1,\ \lambda_2)$.

2) Vegetation Index Calculation: VIs have been applied widely in hyperspectral image classification [42]. According to the relevant literature screening, it was found that these VIs selected in this article indicated the difference in leaf, canopy structure, chlorophyll content, and water content of different wetland plant communities, therefore, these VIs were used in the plant-community classification to improve feature discrimination and accuracy of our target community classes [43]. As given in Table III, these selected VIs indicate the differences in leaf, canopy structure, chlorophyll content, and water content of different wetland plant communities.

3) Texture Features: The features derived from the gray-level co-occurrence matrix (GLCM) are the most commonly used metrics to express the texture features of an image [57]. In this article, we employed the GLCM (15×15 window size) to extract the objects' textural features. These texture features consist of mean, variance, homogeneity, contrast, dissimilarity, entropy, angular second moment, and correlation.

4) Dimensionality Reduction: Principal component analysis (PCA) is a commonly used method of spectral dimensionality reduction. PCA determines a new principal axis for the coordinate system along with the largest possible variance of data [58]. We performed PCA on the processed hyperspectral images and found that the first five principal components after conversion included 99% of the information of all spectral bands.

TABLE III
VEGETATION INDEXES CALCULATED FROM THE UAV HYPERSPECTRAL IMAGERY

Indices	Formulations	References
Simple Ratio	$\frac{R_{842}}{R_{670}}$	[44]
Soil Adjusted Vegetation Index	$\frac{1.5 * (R_{842} - R_{670})}{(R_{842} + R_{670} + 0.5)}$	[45]
Renormalized Difference Vegetation Index	$\frac{(R_{842} - R_{670})}{\sqrt{(R_{842} + R_{670})}}$	[46]
Red Edge Normalized Difference Vegetation Index	$\frac{(R_{754} - R_{702})}{(R_{754} + R_{702})}$	[47]
Optimized Soil Adjusted Vegetation Index	$1.15 * \frac{(R_{798} - R_{670})}{(R_{798} + R_{670} + 0.16)}$	[48]
Triangular Vegetation Index	$0.5[120(R_{750} - R_{550}) - 200(R_{670} - R_{500})]$	[49]
Transformed Chlorophyll Absorption Reflectance Index	$3\left[(R_{702} - R_{670}) - 0.2(R_{702} - R_{550}) * \left(\frac{R_{702}}{R_{670}}\right)\right]$	[50]
ATSAVI	$\frac{1.22(R_{800} - 1.22R_{670} - 0.03)}{[(1.22R_{900} + R_{670} - 1.22 * 0.03 + 0.272)]}$	[51]
Modified Soil Adjusted Vegetation Index	$0.5[2R_{800} + 1 - (2(2R_{800} + 1) - 4(R_{800} - R_{670})]$	[52]
Triangular Greenness Index	$\frac{(R_{670} - R_{480})(R_{670} - R_{550}) - (R_{670} - R_{550})(R_{670} \cdot}{2}$	[53]
Photochemical reflectance index	$(R_{531} - R_{570})/(R_{531} + R_{570})$	[54]
$NDVI_{842}$	$(R_{842} - R_{670})/(R_{842} + R_{670})$	[55]
Enhanced Vegetation Index	$2.5\left(\frac{R_{842} - R_{666}}{R_{842} + 6R_{666} - 7.5R_{480} + 1}\right)$	[56]

Therefore, the first five bands were selected to participate in the classification as spectral feature variables.

F. Classification and Validation

Before the classification step, the RF model was tuned. For the RF algorithm, we assigned a maximum tree growth parameter of 500 to each predictive model [59]. For the CNN algorithm, we propose an eight-layer CNN model that takes spatial and spectral features into account and that consists of an input layer, two convolution layers, two pooling layers, two fully connected layers, and one output layer [60]. For the SVM algorithm, we assigned a gamma (γ) value of zero and a relatively high cost (C) value of 100 [61]. In terms of multiscale segmentation, there are more parameters available for multiscale segmentation in the eCognition software, such as compactness and shape index. However, these two parameters are not available in ENVI software. Therefore, the ENVI 5.5 software was used for pixel-based community classification. And Trimble eCognition Developer 9.3 was used to perform object-based community classification.

The accuracy of this classification output was assessed for each classifier to determine the optimum classifier for classifying wetland plant communities. The evaluation metrics include confusion matrix, overall accuracy (OA), Kappa coefficient, producer accuracy (PA), and user accuracy (UA). OA and the Kappa coefficient are used for the overall classification performance, and PA and UA are used to evaluate individual classes.

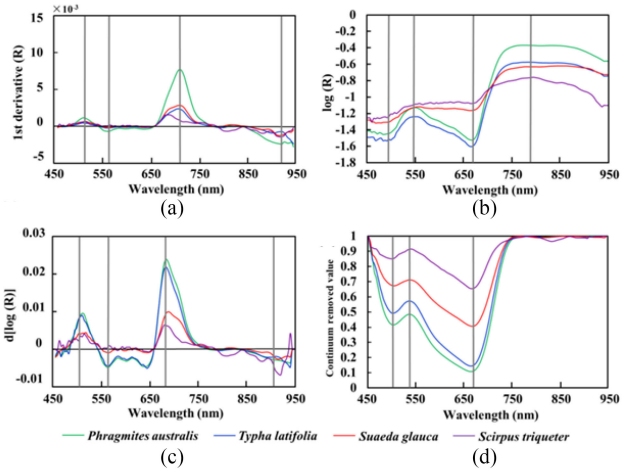

Fig. 4. First-order derivative [d(R)] of the reflectance spectra, the logarithm [log(R)] of the reflectance spectra and its first-order derivative (d[log(R)]) and the continuum removed curves C(R) of the wetland plant communities.

III. RESULTS

A. Spectral Characteristics of Wetland Plant Communities in Momoge Ramsar Site

The mathematical transformation results show that the transformed feature bands highlight the absorption and reflection characteristics of the original spectral reflectance better. As shown in Fig. 4, the spectral curves of the four varieties of wetland plant community share the same positions of peaks and valleys, with increasing reflectance at the "red edge," around 680–720 nm. However, certain differences are observed among the four varieties with respect to the peaks and valleys, and there is overlap among the spectral curves. For example, the first-derivative spectral curves [Fig. 4(a)] in the range of 450–650 nm for *Typha orientalis*, *Suaeda glauca*, and *Scirpus triqueter* almost overlap, making it difficult to distinguish

TABLE IV
SELECTED CHARACTERISTIC WAVELENGTHS IN THIS ARTICLE

Spectral feature	Characteristic wavelengths (nm)
1st derivative	Band 514, Band 558, Band 710, Band 930
log (R)	Band 478, Band 542, Band 674, Band 794
d([log(R)]),	Band 514, Band 562, Band 694, Band 922
C(R)	Band 498, Band 546, Band 674

among wetland plant communities. However, within the range of 650–750 nm, the spectral reflectance of *Phragmites australis* is higher than that of the other three wetland plant communities. At the wavelength position of 674 nm, after a logarithmic transformation [Fig. 4(b)], the curves for *Phragmites australis* and *Typha orientalis* exhibit a relative minimum. Fig. 4(c) shows that there are large differences in the spectra of all the wetland plant communities, especially near the wavelengths of 514, 562, 694, and 992 nm. Fig. 4(d) shows that the absorption features of all types of wetland plant community at 498 and 674 nm have larger amplitude compared with other spectral ranges. The absorption characteristics of these wavelengths have more contrasting power to differentiate among different wetland plant communities. The optimal characteristic wavelength bands are shown in Table IV. These wavelength bands contain the key information needed to distinguish among different wetland plant communities.

B. Accuracy Assessments of Six Classification Schemes

The PA, UA, OA, and Kappa coefficient of different schemes based on the three classifiers are given in Table V. From quantitative accuracy analysis, object-based classifiers have a higher OA than do pixel-based classifiers. The OA of all object-based classification algorithms was higher than 80.29%. Based on object-based classification, the accuracy of the RF classifier was best, with an OA of 87.75% and a Kappa coefficient of 0.864. The OA improved by 4.44% and 7.46%, and the Kappa coefficient improved by 0.035 and 0.051, as compared with CNN and SVM classifiers. According to the comparison and analysis of the classification results, the most-accurately delineated community was *Phragmites australis*. The SVM classifier detected *Phragmites australis* with a PA of 82.76%, while the RF and CNN algorithms tended to distinguish *Phragmites australis* with a very high PA (85.76 and 89.17%, respectively). Note that the dark-colored *Phragmites australis* patches were a source of commission error; and the main source of omission error was dark-colored (low-density) *Phragmites australis* being categorized as *Typha orientalis*. The PA values of the other three types of wetland plant community derived from the object-based RF classifier were also higher than that of the object-based CNN and SVM classification algorithms. For *Scirpus triqueter*, the PA was 80.84%, and the UA was 87.26%, the lowest of all communities. The area of *Scirpus triqueter* is slightly underestimated because this is a relatively rare community type in the study area and relatively few samples are used for training.

When comparing pixel-based classifications, the most accurate map was produced by the CNN algorithm (OA = 74.33%), followed by the RF classifier (OA = 72.69%), while the SVM algorithm had the lowest classification accuracy (OA = 69.42%). The CNN classifier achieved a PA for all types of wetland plant community higher than 70%. The PA of *Typha orientalis* was highest, reaching 79.75%. With regard to the RF and SVM classifiers, the PA values were 66.67 and 62.31%, respectively, for *Typha orientalis*.

Fig. 5 shows the spatial distribution map of wetland plant communities obtained by object-based/pixel-based RF, CNN, and SVM classifiers. As shown in Figs. 5(a), (d), and (g), overall, the object-based classification maps with continuous and homogeneous wetland plant communities especially that produced by the RF classifier, were the most accurate (Table V). For the spatial distribution of each community, the distribution position of most wetland plant communities was consistent with the results of the field investigations. In contrast, the classification results of the pixel-based classification algorithms contain a large amount of pepper noise [Fig. 5(b), (e), and (h)].

C. Geospatial Pattern of Different Wetland Plant Communities

Classification accuracy using optimal feature combination showed that object-based classification results are better than pixel-based classification results (Table V). Post classification field check also showed better accuracy for the object-based classified image. Among the different classification schemes, the object-based RF provided the best results (OA = 87.75%, Kappa = 0.864). The spatial distributions and areas of wetland plant communities of different schemes using RF, CNN, and SVM classifiers are shown in Fig. 5. The total study area is 518.33 ha. *Phragmites australis* and *Typha orientalis* are the dominant community types, accounting for 57–67% (295–346 ha) and 11–16% (57–84 ha) of the total area, respectively, corresponding to a total of 68–83% of the study area [Fig. 5(c), (f), and (i)]. Communities dominated by *Phragmites australis* were the most spatially abundant and distributed in the whole study site, followed by *Typha orientalis* and *Suaeda glauca*. *Typha orientalis* was concentrated mainly in the southern and northern regions. *Suaeda glauca* and *Scirpus triqueter* covered 11–15% (57–79 ha) and 2–5% (8–26 ha) [Fig. 5(c), (f), and (i)], corresponding to a total of 13–20% of the study area. *Scirpus triqueter* was the least-representative class and distributed between *Typha orientalis* and *Phragmites australis*, covering only 5% of the study area. *Suaeda glauca* was concentrated mainly in the west and north of the study area.

IV. DISCUSSION

A. Advantages of UAV Hyperspectral Imagery for Mapping Wetland Plant Communities

Wetlands are heterogeneous ecosystems containing wetland plant community patches with similar spectral responses, which may cause spectral confusion [62]. Besides, the spatial distributions and growth densities of different wetland plant communities differ. Mapping wetland plant communities with traditional optical remote sensing is challenging because of the few wavebands used by optical sensors. This limits the ability to

TABLE V
COMPARISON OF CLASSIFICATION ACCURACY FOR EACH COMMUNITY ON DIFFERENT CLASSIFICATION SCHEMES

Classified Category	RF (Object-Based)		RF (Pixel-Based)		CNN (Object-Based)		CNN (Pixel-Based)		SVM (Object-Based)		SVM (Pixel-Based)	
	PA	UA	PA	UA	PA	UA	PA	UA	PA	UA	PA	UA
Phragmites australis	89.17	88.06	74.22	80.15	85.76	85.48	76.59	78.62	82.76	94.55	70.73	89.51
Typha orientalis	81.93	80.20	66.67	73.57	80.36	98.23	79.75	85.38	79.96	89.03	62.31	80.77
Suaeda glauca	83.22	82.13	71.43	80.18	82.67	97.48	74.52	95.47	77.11	87.88	65.88	75.49
Scirpus triqueter	80.84	87.26	64.52	72.52	75.62	79.94	71.43	98.68	72.80	83.59	64.19	72.80
Water	100.00	100.00	100.00	99.98	100.00	100.00	100.00	99.85	100.00	100.00	100.00	99.88
Bare land	98.80	93.64	87.28	100.00	91.74	85.55	90.53	94.76	84.50	90.61	83.74	90.43
OA(%)	87.75		72.69		83.31		74.33		80.29		69.42	
Kappa	0.864		0.705		0.829		0.797		0.813		0.690	

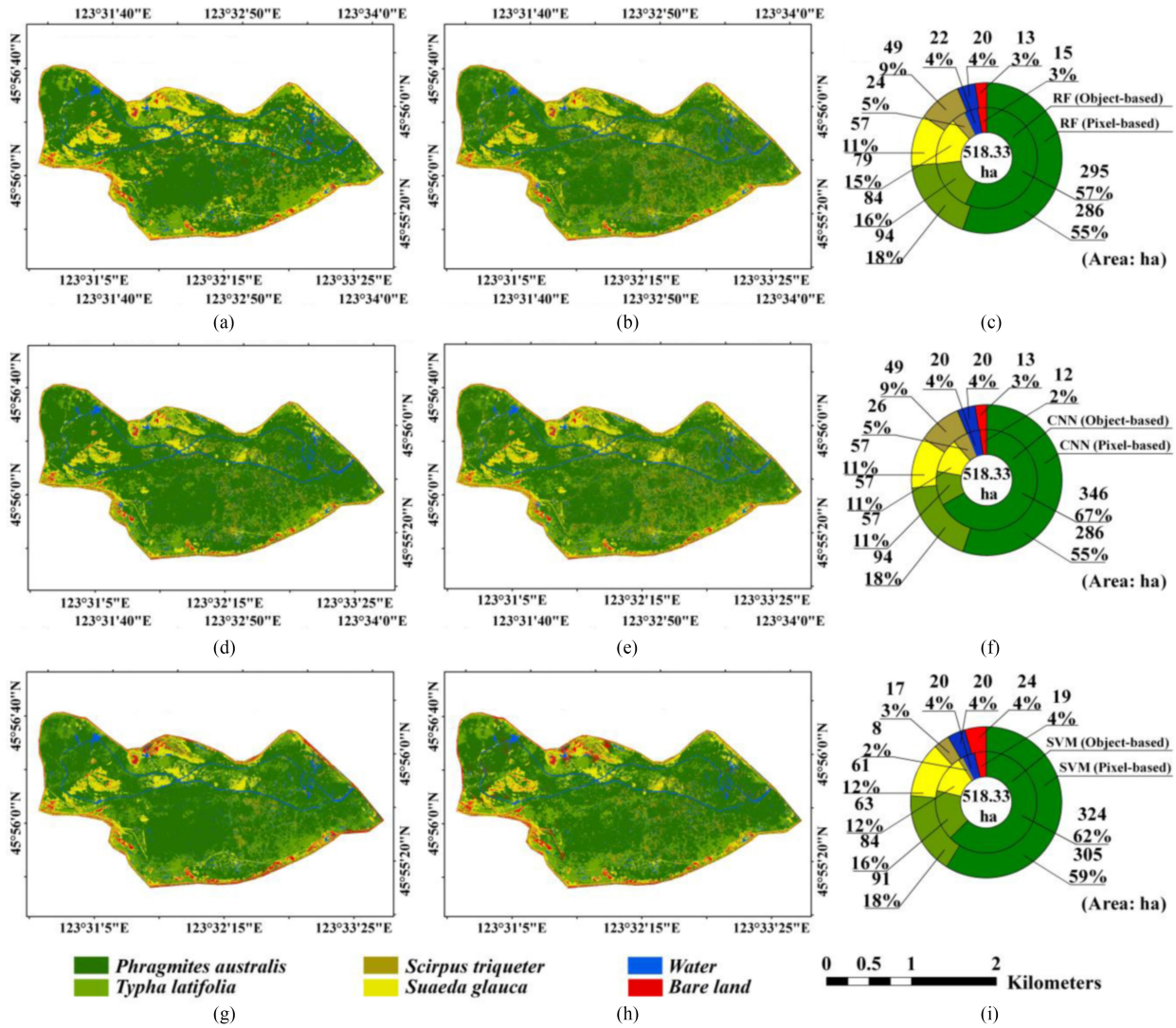

Fig. 5. Distribution of the wetland plant communities and pie charts presents the areal statistics of the community area identified based on different classification algorithms at the study site: (a) object-based RF and (b) pixel-based RF classification algorithms; (d) object-based CNN and (e) pixel-based CNN classification algorithms; (g) object-based SVM and (h) pixel-based SVM classification algorithms; (c), (f), and (i) are the statistics of the community area of different classification schemes.

discriminate among plant communities based on the reflection and absorption of light using these few channels [8].

Compared with space-borne hyperspectral data, UAV hyperspectral data have great advantages when finely mapping wetland plant communities [63]. Because of the typically low flying height involved, the resolution of images obtained by UAV hyperspectral sensors can reach 5–10 cm or less, which means that UAV hyperspectral images have both hyperspectral and high spatial characteristics, providing an important data source for wetland plant monitoring [13]. Several hyperspectral studies of wetland plant mapping have found that UAV hyperspectral remote sensing focuses mainly on coastal wetlands

Fig. 6. *Phragmites australis* communities in different growth environments. (a) *Phragmites australis* with high coverage. (b) *Phragmites australis* seedlings with low coverage. (c) Variation in leaf angles of the canopy of *Phragmites australis* communities.

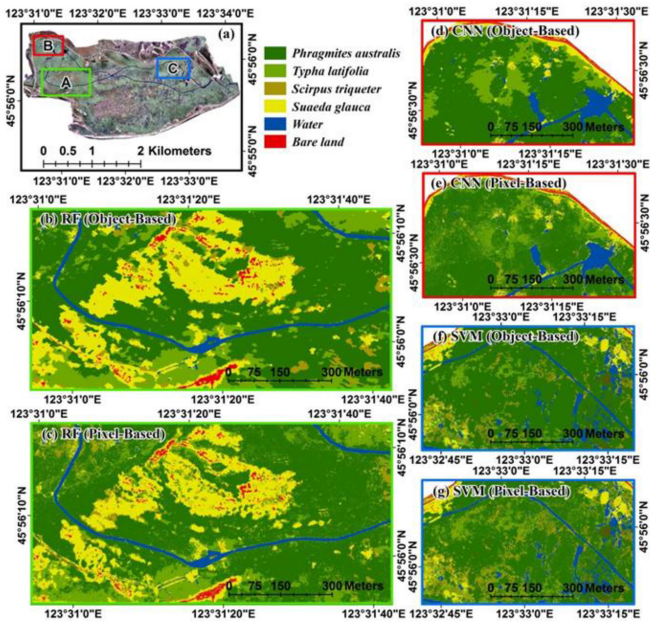

Fig. 7. Local-enlarged views of the overall coverage maps of different schemes using the RF, CNN, and SVM classifiers.

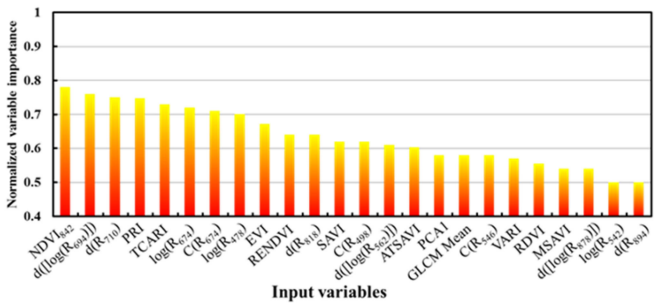

Fig. 8. Evaluation of input variable importance in object-based RF Classification.

classification, invasion of alien vegetation, wetland mapping, and coastal sediment grain size monitoring [64]. In this article, we combined a new UAV remote sensing platform with a new remote sensor in a high hyperspectral imaging instrument. From the classification results, UAV hyperspectral imagery performs well in classifying wetland plant communities, and this could be useful for identifying the health status at species or community level.

B. Comparison of Classification Results Based on Object-Based and Pixel-Based Classification Methods

In this article, UAV hyperspectral imagery with centimeter-level resolution provides rich spatial features. The spatial information of different wetland plant communities is highly detailed, and the spectra overlap with each other. As shown in Fig. 6, the spectral features of *Phragmites australis* may be very complex because *Phragmites australis* can grow in different environments. Therefore, spectral variations can also occur within a species because of differences in age, leaf water content, leaf angle distribution, soil and water background, and other structural characteristics. As shown in Fig. 7(c), (e), and (g), pixel-based classifications produce lower accuracies with a salt-and-pepper look. Overall, the object-based approach alleviated this problem by aggregating pixels into larger image objects and prevented the formation of such extraneous tiny patches. Which are crucial in discriminating between different wetland plant communities with similar spectral response characteristics. As shown in Figs. 7(b), (d), and (f), the object-based distribution maps of wetland plant communities have greater homogeneous areas. Moreover, the classified images are much cleaner, and the classified areas are visually more similar to real-world objects compared with the pixel-based distribution maps. According to the comparison of the classification results (Table V), the object-based approach outperformed the pixel-based approach for most cases (an improved OA of 9–15%).

C. Performance of Different Machine-Learning Algorithms and Classification Features

In this article, object- and pixel-based classification was used to classify wetland plant communities, and the classification effects of the three classifiers were compared and analyzed. As shown in Table V and Fig. 7, this article concludes that the object-based RF classification algorithm achieved the highest OA (87.75%) of all the compared classification algorithms. The classification accuracies for all wetland plant communities were greater than 80% in terms of PA and UA. In contrast, the object-based CNN and SVM classifiers generated a slightly lower OA (83.31 and 80.29%, respectively). Most previous studies have shown that the classification performance of the CNN classifier is better than that of the RF classifier [65], [66], while the results obtained in this article do not seem to be consistent with the results of previous studies. For CNN, this article shows that feature subsets cannot provide more-accurate classification results. One possible explanation for this could be that the CNN classifier did not learn more feature variables. For object-based RF classification algorithm, classifier performance and efficiency can be improved by eliminating redundant features. Apart from this, CNN depends heavily on the quantity and quality of the labeled samples. In this article, the training and validation samples were selected from typical locations that people could access. For sites away from roads, only limited training or validation samples were collected based on the vegetation distribution rules and local knowledge.

An advantage of the RF algorithm is that it allows the quantification of the importance of each feature variable used

in the classification. Fig. 8 shows that there are eight most important features, whose contribution ratio is higher than 0.7. Among them, the five most important input features are selected using a mathematical transformation in the red-edge region. Specifically, $NDVI_{842}$ is critical for importance evaluation in all features. Additionally, the contribution ratio of the first-order derivative d(R) and its first-order derivative d[log(R)] of the red-edge region (674, 694, and 710 nm) is also in an important position. This also proves the transformation analysis results of hyperspectral imagery (Fig. 5). The greatest differences among these wetland plant communities regarding canopy reflectance are in the red and red-edge regions (650–750 nm), followed by the green region (500–570 nm) and the near-infrared region (800–900 nm).

V. Conclusion

Taking heed of inland wetland plant community monitoring requirements, we used UAV hyperspectral imagery for wetland plant community classification. On the basis of feature selection and feature combination, we compared the performance of three machine-learning techniques, i.e., the RF, CNN, and SVM classifiers, regarding pixel/object-based classification. The object-based classification improved the classification accuracy (up to 9–15%) and avoided the phenomenon of "salt and pepper." RF performed better than the other two classifiers, i.e., CNN and SVM, in terms of its OA of 87.75%, followed by the OAs of 83.31 and 80.29%, respectively. The high accuracy of RF was believed to be a result of the effective data transformation, as well as the combination of spatial information in the classification. Specifically, the spectral transformation features in the red-edge region can effectively distinguish different wetland plant communities. As a result, the complexity of the model training process was simplified, and the processing time required for supervised classification was reduced significantly. In future studies, we need to explore the contribution of different feature combinations in the process of community classification.

Acknowledgment

The author would like to thank Prof. Dehua Mao for proofreading the manuscript. The author would like to thank the graduate students involved infield data collection. Author also want to thank the reviewers who helped to improve the article.

References

[1] T. Kumar, A. Mandal, D. Dutta, R. Nagaraja, and V. K. Dadhwal, "Discrimination and classification of mangrove forests using EO-1 hyperion data: A case study of Indian Sundarbans," *Geocarto Int.*, vol. 34, pp. 415–442, Mar. 2019.

[2] Y. Wang, J. Feng, Q. X. Lin, X. G. Lyu, X. Y. Wang, and G. P. Wang, "Effects of crude oil contamination on soil physical and chemical properties in momoge wetland of China," *Chin. Geographical Sci.*, vol. 23, pp. 708–715, Dec. 2013.

[3] L. Mabhungu, E. Adam, and S. W. Newete, "Monitoring of phytoremediating wetland macrophytes using remote sensing: The case of common reed (phragmites australis (Cav.) Trin. Ex steud.) and the giant reed (Arundo donax L.). A review," *Appl. Ecol. Environ. Res.*, vol. 17, pp. 7957–7972, 2019.

[4] D. H. Mao *et al.*, "Conversions between natural wetlands and farmland in China: A multiscale geospatial analysis," *Sci. Total Environ.*, vol. 634, pp. 550–560, Sep. 2018.

[5] E. Underwood, M. Mulitsch, J. Greenberg, M. Whiting, S. Ustin, and S. Kefauver, "Mapping invasive aquatic vegetation in the sacramento-san joaquin delta using hyperspectral imagery," *Environ. Monit. Assessment*, vol. 121, pp. 47–64, 2006.

[6] M. Grenier, S. Labrecque, M. Garneau, and A. Tremblay, "Object-based classification of a SPOT-4 image for mapping wetlands in the context of greenhouse gases emissions: The case of the eastmain region, Quebec, Canada," *Can. J. Remote Sens.*, vol. 34, pp. S398–S413, 2008.

[7] M. Laba *et al.*, "Mapping invasive wetland plants in the Hudson River National Estuarine Research Reserve using quickbird satellite imagery," *Remote Sens. Environ.*, vol. 112, pp. 286–300, Jan. 2008.

[8] Y. Zhang, D. Lu, B. Yang, C. Sun, and M. Sun, "Coastal wetland vegetation classification with a landsat thematic mapper image," *Int. J. Remote Sens.*, vol. 32, pp. 545–561, 2011.

[9] J. Boyden, K. E. Joyce, G. Boggs, and P. Wurm, "Object-based mapping of native vegetation and para grass (Urochloa mutica) on a monsoonal wetland of Kakadu NP using a landsat 5 TM dry-season time series," *J. Spatial Sci.*, vol. 58, pp. 53–77, 2013.

[10] J. Verrelst, G. W. Geerling, K. V. Sykora, and J. G. P. W. Clevers, "Mapping of aggregated floodplain plant communities using image fusion of CASI and LiDAR data," *Int. J. Appl. Earth Observ. Geoinf.*, vol. 11, pp. 83–94, Feb. 2009.

[11] E. Adam, N. Mureriwa, and S. Newete, "Mapping Prosopis glandulosa (mesquite) in the semi-arid environment of South Africa using high-resolution worldview-2 imagery and machine learning classifiers," *J. Arid Environ.*, vol. 145, pp. 43–51, Oct. 2017.

[12] L. Kumar and P. Sinha, "Mapping salt-marsh land-cover vegetation using high-spatial and hyperspectral satellite data to assist wetland inventory," *GISci. Remote Sens.*, vol. 51, pp. 1–16, 2014.

[13] J. Harken and R. Sugumaran, "Classification of Iowa wetlands using an airborne hyperspectral image: A comparison of the spectral angle mapper classifier and an object-oriented approach," *Can. J. Remote Sens.*, vol. 31, pp. 167–174, Apr. 2005.

[14] R. J. Zomer, A. Trabucco, and S. L. Ustin, "Building spectral libraries for wetlands land cover classification and hyperspectral remote sensing," *J. Environ. Manage.*, vol. 90, pp. 2170–2177, May 2009.

[15] V. Klemas, "Remote sensing of coastal wetland biomass: An overview," *J. Coastal Res.*, vol. 29, pp. 1016–1028, Sep. 2013.

[16] Y. Ma, J. Zhang, and J. Y. Zhang, "Analysis of unmanned aerial vehicle (UAV) hyperspectral remote sensing monitoring key technology in coastal wetland," in *Proc. Sel. Papers Photoelectron. Technol. Committee Conf.*, 2016, Art. no. 97962S.

[17] E. A. L. Salas and S. K. Subburayalu, "Modified shape index for object-based random forest image classification of agricultural systems using airborne hyperspectral datasets," *Plos One*, vol. 14, Mar. 2019, Art. no. e0213356.

[18] Y. Cao, K. Jiang, J. Wu, F. Yu, W. Du, and T. Xu, "Inversion modeling of japonica rice canopy chlorophyll content with UAV hyperspectral remote sensing," *PLoS One*, vol. 15, 2020, Art. no. e0238530.

[19] C. Sothe *et al.*, "Tree species classification in a highly diverse subtropical forest integrating UAV-based photogrammetric point cloud and hyperspectral data," *Remote Sens.*, vol. 11, Jun. 2019, Art. no. 1338.

[20] X. Zhou, J. Sun, Y. Tian, Q. S. Chen, X. H. Wu, and Y. Y. Hang, "A deep learning based regression method on hyperspectral data for rapid prediction of cadmium residue in lettuce leaves," *Chemometrics Intell. Lab. Syst.*, vol. 200, May 2020, Art. no. 103996.

[21] J. J. Cao, W. C. Leng, K. Liu, L. Liu, Z. He, and Y. H. Zhu, "Object-based mangrove species classification using unmanned aerial vehicle hyperspectral images and digital surface models," *Remote Sens.*, vol. 10, Jan. 2018, Art. no. 89.

[22] B. P. Banerjee, S. Raval, and P. J. Cullen, "UAV-hyperspectral imaging of spectrally complex environments," *Int. J. Remote Sens.*, vol. 41, pp. 4136–4159, Jun. 2020.

[23] J. N. Wang, L. F. Zhang, and Q. X. Tong, "The derivative spectral matching for wetland vegetation identification and classification by hyperspectral data," *Hyperspectral Remote Sens. Appl.*, vol. 3502, pp. 280–288, 1998.

[24] Y. A. Yan, L. Deng, X. L. Liu, and L. Zhu, "Application of UAV-based multi-angle hyperspectral remote sensing in fine vegetation classification," *Remote Sens.*, vol. 11, Dec. 2019, Art. no. 2753.

[25] L. White, R. A. Ryerson, J. Pasher, and J. Duffe, "State of science assessment of remote sensing of Great Lakes coastal wetlands: Responding to an operational requirement," *Remote Sens.*, vol. 12, Sep. 2020, Art. no. 3024.

[26] J. R. Harris and E. C. Grunsky, "Predictive lithological mapping of Canada's north using random forest classification applied to geophysical and geochemical data," *Comput. Geosci.*, vol. 80, pp. 9–25, Jul. 2015.

[27] N. K. Poona, A. van Niekerk, R. L. Nadel, and R. Ismail, "Random forest (RF) wrappers for waveband selection and classification of hyperspectral data," *Appl. Spectrosc.*, vol. 70, pp. 322–333, Feb. 2016.

[28] X. C. Zhou, S. L. Li, F. Tang, K. Qin, S. D. Hu, and S. J. Liu, "Deep learning with grouped features for spatial spectral classification of hyperspectral images," *IEEE Geosci. Remote Sens. Lett.*, vol. 14, no. 1, pp. 97–101, Jan. 2017.

[29] A. M. Abdi, "Land cover and land use classification performance of machine learning algorithms in a boreal landscape using Sentinel-2 data," *Gisci. Remote Sens.*, vol. 57, pp. 1–20, Jan. 2020.

[30] G. P. Petropoulos, C. Kalaitzidis, and K. P. Vadrevu, "Support vector machines and object-based classification for obtaining land-use/cover cartography from hyperion hyperspectral imagery," *Comput. Geosci.*, vol. 41, pp. 99–107, Apr. 2012.

[31] T. Abeysinghe *et al.*, "Mapping invasive phragmites australis in the old woman creek estuary using UAV remote sensing and machine learning classifiers," *Remote Sens.*, vol. 11, Jun. 2019, Art. no. 1380.

[32] Y. Q. Chen, S. J. Qiao, G. X. Zhang, Y. J. Xu, L. W. Chen, and L. L. Wu, "Investigating the potential use of Sentinel-1 data for monitoring wetland water level changes in China's Momoge National Nature Reserve," *Peer J.*, vol. 8, Feb. 2020, Art. no. e8616.

[33] Y. Zhang *et al.*, "Changes in habitat suitability for waterbirds of the Momoge Nature Reserve of China during 1990-2014," *J. Environ. Eng. Landscape Manage.*, vol. 25, pp. 367–378, 2017.

[34] H. B. Jiang, Y. Wen, L. F. Zou, Z. Q. Wang, C. G. He, and C. L. Zou, "The effects of a wetland restoration project on the siberian crane (Grus leucogeranus) population and stopover habitat in Momoge National Nature Reserve, China," *Ecol. Eng.*, vol. 96, pp. 170–177, Nov. 2016.

[35] H. Aasen and A. Bolten, "Multi-temporal high-resolution imaging spectroscopy with hyperspectral 2D imagers—From theory to application," *Remote Sens. Environ.*, vol. 205, pp. 374–389, 2018.

[36] H. Aasen, J. Bendig, A. Bolten, S. Bennertz, M. Willkomm, and G. Bareth, "Introduction and preliminary results of a calibration for full-frame hyperspectral cameras to monitor agricultural crops with UAVs," in *Proc. ISPRS Tech. Commission VII Symp.*, 2014, pp. 1–8.

[37] J. Yue *et al.*, "Estimation of winter wheat above-ground biomass using unmanned aerial vehicle-based snapshot hyperspectral sensor and crop height improved models," *Remote Sens.*, vol. 9, 2017, Art. no. 708.

[38] N. Zhang, Y. Wang, and X. Zhang, "Extraction of tree crowns damaged by Dendrolimus Tabulaeformis Tsai et Liu via spectral-spatial classification using UAV-based hyperspectral images," *Plant Methods*, vol. 16, 2020, Art. no. 135.

[39] D. M. Meneguzzo, G. C. Liknes, and M. D. Nelson, "Mapping trees outside forests using high-resolution aerial imagery: A comparison of pixel- and object-based classification approaches," *Environ. Monit. Assessment*, vol. 185, pp. 6261–6275, Aug. 2013.

[40] M. Liu *et al.*, "Rapid invasion of spartina alterniflora in the coastal zone of mainland China: New observations from landsat OLI images," *Remote Sens.*, vol. 10, 2018, Art. no. 1933.

[41] M. Liu *et al.*, "The impact of spatial resolution on the classification of vegetation types in highly fragmented planting areas based on unmanned aerial vehicle hyperspectral images," *Remote Sens.*, vol. 12, Jan. 2020, Art. no. 146.

[42] T. Adao *et al.*, "Hyperspectral imaging: A review on UAV-based sensors, data processing and applications for agriculture and forestry," *Remote Sens.*, vol. 9, Nov. 2017, Art. no. 1110.

[43] Y. S. Wu and X. L. Zhang, "Object-based tree species classification using airborne hyperspectral images and LiDAR data," *Forests*, vol. 11, Jan. 2020, Art. no. 32.

[44] G. S. Birth and G. R. McVey, "Measuring the color of growing turf with a reflectance spectrophotometer1," *Agronomy J.*, vol. 60, pp. 640–643, 1968.

[45] A. R. Huete, "A soil-adjusted vegetation index (SAVI)," *Remote Sens. Environ.*, vol. 25, pp. 295–309, 1988.

[46] J.-L. Roujean and F.-M. Breon, "Estimating PAR absorbed by vegetation from bidirectional reflectance measurements," *Remote Sens. Environ.*, vol. 51, pp. 375–384, 1995.

[47] A. A. Gitelson, M. N. Merzlyak, and H. K. Lichtenthaler, "Detection of red edge position and chlorophyll content by reflectance measurements near 700 nm," *J. Plant Physiol.*, vol. 148, pp. 501–508, 1996.

[48] G. Rondeaux, M. Steven, and F. Baret, "Optimization of soil-adjusted vegetation indices," *Remote Sens. Environ.*, vol. 55, pp. 95–107, 1996.

[49] N. H. Broge and E. Leblanc, "Comparing prediction power and stability of broadband and hyperspectral vegetation indices for estimation of green leaf area index and canopy chlorophyll density," *Remote Sens. Environ.*, vol. 76, pp. 156–172, 2001.

[50] D. Haboudane, J. R. Miller, N. Tremblay, P. J. Zarco-Tejada, and L. Dextraze, "Integrated narrow-band vegetation indices for prediction of crop chlorophyll content for application to precision agriculture," *Remote Sens. Environ.*, vol. 81, pp. 416–426, 2002.

[51] F. Baret and G. Guyot, "Potentials and limits of vegetation indices for LAI and APAR assessment," *Remote Sens. Environ.*, vol. 35, pp. 161–173, 1991.

[52] J. Qi, A. Chehbouni, A. R. Huete, Y. H. Kerr, and S. Sorooshian, "A modified soil adjusted vegetation index," *Remote Sens. Environ.*, vol. 48, pp. 119–126, 1994.

[53] E. R. Hunt, C. S. T. Daughtry, J. U. H. Eitel, and D. S. Long, "Remote sensing leaf chlorophyll content using a visible band index," *Agronomy J.*, vol. 103, pp. 1090–1099, 2011.

[54] R. Hernández-Clemente, R. M. Navarro-Cerrillo, L. Suárez, F. Morales, and P. J. Zarco-Tejada, "Assessing structural effects on PRI for stress detection in Conifer forests," *Remote Sens. Environ.*, vol. 115, pp. 2360–2375, 2011.

[55] J. J. Cao K. Liu, L. Liu, Y. H. Zhu, J. Li, and Z. He, "Identifying mangrove species using field close-range snapshot hyperspectral imaging and machine-learning techniques," *Remote Sens.*, vol. 10, Dec. 2018, Art. no. 2047.

[56] A. Huete, K. Didan, T. Miura, E. P. Rodriguez, X. Gao, and L. G. Ferreira, "Overview of the radiometric and biophysical performance of the MODIS vegetation indices," *Remote Sens. Environ.*, vol. 83, pp. 195–213, 2002.

[57] R. S. Majdar and H. Ghassemian, "A probabilistic framework for weighted combination of multiple-feature classifications of hyperspectral images," *Earth Sci. Informat.*, vol. 13, pp. 55–69, Mar. 2020.

[58] W. X. Yin, C. Zhang, H. Y. Zhu, Y. R. Zhao, and Y. He, "Application of near-infrared hyperspectral imaging to discriminate different geographical origins of Chinese wolfberries," *Plos One*, vol. 12, Jul. 2017, Art. no. e0180534.

[59] Y. T. Cai, H. Lin, and M. Zhang, "Mapping paddy rice by the object-based random forest method using time series Sentinel-1/Sentinel-2 data," *Adv. Space Res.*, vol. 64, pp. 2233–2244, Dec. 2019.

[60] Q. Yue and C. W. Ma, "Deep learning for hyperspectral data classification through exponential momentum deep convolution neural networks," *J. Sensors*, vol. 2016, 2016, Art. no. 3150632.

[61] M. S. Colgan, C. A. Baldeck, J. B. Feret, and G. P. Asner, "Mapping savanna tree species at ecosystem scales using support vector machine classification and BRDF correction on airborne hyperspectral and LiDAR data," *Remote Sens.*, vol. 4, pp. 3462–3480, Nov. 2012.

[62] E. Adam, O. Mutanga, and D. Rugege, "Multispectral and hyperspectral remote sensing for identification and mapping of wetland vegetation: A review," *Wetlands Ecol. Manage.*, vol. 18, pp. 281–296, Jun. 2010.

[63] T. T. Sankey, J. McVay, T. L. Swetnam, M. P. McClaran, P. Heilman, and M. Nichols, "UAV hyperspectral and lidar data and their fusion for arid and semi-arid land vegetation monitoring," *Remote Sens. Ecol. Conservation*, vol. 4, pp. 20–33, Mar. 2018.

[64] D. H. Mao *et al.*, "Rapid invasion of Spartina Alterniflora in the coastal zone of mainland China: Spatiotemporal patterns and human prevention," *Sensors*, vol. 19, May 2019, Art. no. 2308.

[65] M. E. Paoletti, J. M. Haut, J. Plaza, and A. Plaza, "Deep learning classifiers for hyperspectral imaging: A review," *ISPRS J. Photogramm. Remote Sens.*, vol. 158, pp. 279–317, Dec. 2019.

[66] M. S. Roodposhti, J. Aryal, A. Lucieer, and B. A. Bryan, "Uncertainty assessment of hyperspectral image classification: Deep learning vs. random forest," *Entropy*, vol. 21, Jan. 2019, Art. no. 78.